Aperture synthesis imaging of ionospheric irregularities using time diversity MIMO radar

D. L. Hysell[1] and J. L. Chau[2]

[1]Earth and Atmospheric Sciences, Cornell University, Ithaca, NY, USA
[2]Leibniz Institute of Atmospheric Physics at the University of Rostock, Külungsborn, Germany

Key Points:

- Multiple-input, multiple output (MIMO) radar imaging method implemented at Jicamarca to observe large-scale waves in the EEJ.
- Specific method involves time division multiplexing or time diversity.
- The resolution of the images was increased but is limited by motion of scatterers which needs mitigation.

Corresponding author: D. L. Hysell, `david.hysell@cornell.edu`

Abstract

Aperture-synthesis images of ionospheric irregularities in the equatorial electrojet are computed using multiple-input multiple-output (MIMO) radar methods at the Jicamarca Radio Observatory. MIMO methods increase the number of distinct interferometry baselines available for imaging (by a factor of essentially three in these experiments) as well as the overall size of the synthetic aperture. The particular method employed here involves time-division multiplexing or time diversity to distinguish pulses transmitted from different quarters of the Jicamarca array. The method comes at the cost of a large increase in computation time and complexity and a reduced signal-to-noise ratio. We discuss the details involved in the signal processing and the trade space involved in image optimization.

1 Introduction and motivation

Aperture synthesis imaging (ASI) is a powerful technique with origins in radio astronomy that enables the construction of high-resolution images of celestial sources with high accuracy and precision. The technique involves combining the signals collected by multiple radio telescopes arranged in a strategic configuration, forming a virtual dish with an aperture equivalent to the maximum separation between the outermost telescopes. By measuring the visibilities (complex cross correlations) obtained from these signals, which encode the spatial frequency content of the image, the technique can be used to produce detailed images of the source with the incorporation of statistical inverse methods. The resulting images offer detailed renderings of astrophysical phenomena while providing access to physical parameters that can elucidate the underlying physics. For a review, see Thompson et al. (2017).

Aperture synthesis imaging was introduced to the field of radar aeronomy by Kudeki and Sürücü (1991) who were studying backscatter from plasma density irregularities in the equatorial electrojet (EEJ) above the Jicamarca Radio Observatory outside Lima, Peru. Conventional radar methods, including interferometry, suggested the presence of large-scale (kilometer-scale) waves in the EEJ with phase speeds and wavelengths that varied according to the time of day (see for example Farley et al., 1981). ASI offered a direct, unambiguous means of observing and characterizing these waves, producing imagery directly comparable with numerical simulations that were emerging at about the same time (Ronchi et al., 1989, 1991). More sophisticated inverse methods would later be applied to the data inversion, giving rise to sharper images with reduced artifacts (see e.g., Hysell & Chau, 2006, and references therein). Imaging would go on to be used to investigate irregularities in other altitude strata over Jicamarca as well as ionospheric phenomena at different longitudes and at middle and high latitudes (e.g., Hysell et al., 2002; Bahcivan et al., 2006; Larsen et al., 2007; Saito et al., 2008; Hysell & Chau, 2012; Harding & Milla, 2013; Sommer & Chau, 2016; Chau et al., 2020; Bui et al., 2023; He et al., 2023).

Jicamarca is especially suitable for aperture synthesis methods because of the modularity of its main phased-array antenna which can be divided into different modules for reception, each with an area 1/64 the main array. Radar studies conducted there can therefore exploit experimental degrees of freedom associated with range, time, Doppler frequency, and the spatial diversity of the receive antennas.

Recently, the idea of exploiting the spatial diversity of antennas used for transmission was also introduced to radar aeronomy (Urco et al., 2018). The work can be viewed as an application of multiple-input, multiple-output (MIMO) signal processing as has been widely applied in areas such as wireless communications (e.g., Zheng & Tse, 2003), maritime radar navigation (Huang et al., 2011) and over the horizon radar (Frazer et al., 2007). To exploit spatial diversity of antennas on radar applications, different diversity schemes on transmission can be applied depending on the target characteristics and the system capabilities. Examples of radar diversity are time, frequency, polarization, and code.

In aeronomy research, MIMO radar to improve radar interferometry has been focused on multistatic meteor radars using relatively small transmitting arrays (Chau et al., 2019). These systems called SIMONe (Spread Spectrum Interferometric Multistatic meteor radar Observing Network) make use of code diversity to implement MIMO and estimate winds at mesospheric and lower thermospheric (MLT) altitudes, where a relatively large number of meteor trails can be used to measure line of sight neutral wind projections from different fields of view. The same SIMONe systems have been also used to measure ionospheric irregularities where imaging can be performed assuming one target in a given range, time and Doppler bin (Chau et al., 2021; Huyghebaert et al., 2022). MIMO in radar aeronomy research has also been applied to study atmospheric processes. For example, Matsuda and Hashiguchi (2023) has implemented MIMO at the MU radar using frequency diversity to reduce the beam broadening effect in turbulence measurements while Urco et al. (2019) used time diversity at MAARSY to remove spatial and temporal ambiguities on polar mesospheric summer echoes. Time diversity was implemented since it was not possible to implement code diversity at MAARSY.

In this paper, we follow on Urco et al. (2018) and incorporate time-diversity MIMO into an aperture synthesis imaging framework. This is readily accomplished at Jicamarca where transmission can take place separately on individual quarters of the main antenna array. For a target, we return to coherent scatter from irregularities in the EEJ and signatures of large-scale waves within. The goal of MIMO imaging is to increase significantly the number of interferometry baselines and visibility measurements available without relying on additional hardware or construction. The method, its implementation, its drawbacks, and the overall optimization trade space is discussed below.

2 MIMO imaging methods using time diversity

The methodology for imaging ionospheric plasma density irregularities with a pulsed monostatic coherent scatter radar was established at Jicamarca in the 1990s (Kudeki & Sürücü, 1991; Hysell, 1996). Pulses are emitted by the radar at regular intervals denoted by the interpulse period (IPP) which is chosen to avoid range and frequency aliasing. (Targets for which both can be avoided simultaneously are called "underspread" and are the main concern of this paper.) Samples of the echoes are recorded continuously at a rate matched to the bandwidth of the emitted pulses. The data yielded by the receivers are quadrature baseband voltage samples from multiple spaced antennas. Preliminary data processing is used to convert these samples to estimates of all possible cross-spectra permutations afforded by the various receivers, and these estimates form the basis for imaging. This preliminary processing includes matched filtering of the baseband samples from each receiver. The emitted waveforms used for coherent scatter generally employ binary phase codes, and the filtering is matched to the code. In the case of the experiments considered here, the code used was a 28-bit maximum length code with a bit width of 1 μs and an IPP of 1 ms. The corresponding duty cycle is 2.8%, and the range resolution is 150 m. **The relatively high compression ratio of the pulse code use here is necessary in view of the requirement for a very high signal-to-noise ratio combined with the bandwidth needed to resolve the ionospheric target in range.**

Spectral analysis is then performed on the time series samples from each receiver to convert them from the time to the Doppler frequency domain. The analysis is performed with discrete Fourier transforms. We typically employ zero padding to remove artifacts associated with discontinuities at the start/end of the data window. The number of spectral bins considered is chosen to optimize the balance between spectral resolution and the overall measurement cadence. The E region irregularities in the sampling volume over Jicamarca considered for this work evolve on timescales of a few seconds, and this fixes the upper limit on the incoherent integration time used in the estimation of the cross spectra. For these experiments, we consider 22 spectral bins and an overall incoherent integration time of 5 s. **The spectral bandwidth of the overall experiment described below will encompass Doppler shifts between $\pm$ 375 m/s.**

Interferometry is performed by computing the normalized cross-spectra for all the possible permutations of signals from the receiving antennas. The complex normalized cross spectra or visibility measurement that can be formed from the signals v^i, v^j from antennas i and j can be designated V^{ij}. Given N spaced antennas, as many as $N(N-1)/2$ distinct interferometry baselines are available, or $N(N-1)/2+1$ including the zero (repeated index) baseline. For the illustrative purposes, we consider in Fig. 1 the case of $N=2$ with the two receive antennas designated by the numbers 1 and 2.

The distinguishing characteristic of MIMO experiments is the use of multiple, spatially-separated transmitting antennas. In the case of the present experiments, we transmitted pulses on either the west or the east quarter of the main antenna at Jicamarca. Displacing the transmitting antenna spatially in an interferometry experiment has the equivalent effect of displacing the receive antennas in the opposite direction. The baselines formed by correlating signals associated with different transmission locations are consequently offset by the spatial separation of the transmitters. **(Note that we are mainly interested in studying backscatter from magnetic field-aligned plasma density irregularities here for which numerous and long east-west interferometry baselines are the most informative.)**

In Fig. 1, arrows represent interferometry baselines associated with visibilities V_{xy}^{ij} for signals originating from transmitting antennas x and y and acquired with receiving antennas i and j. 'E' and 'W' denote east and west, respectively. The black arrows represent interferometry baselines in SIMO

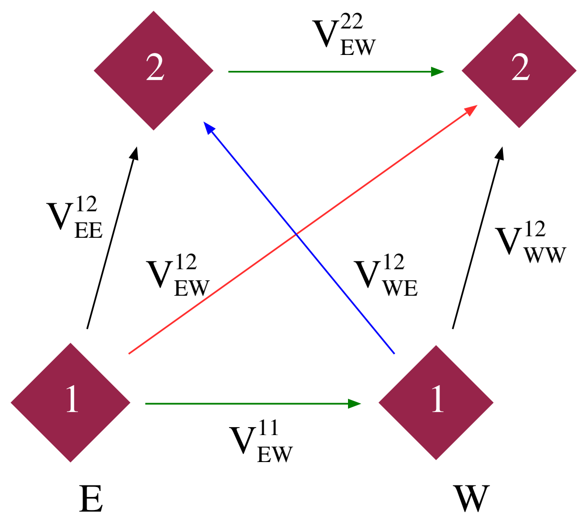

Figure 1. Diagram illustrating visibility measurements in a generalized MIMO experiment involving two transmitting antennas separated east-west (not drawn). We consider two hypothetical receive antennas numbered 1 and 2. The black arrows represent the interferometry baseline for SIMO data collection when signals transmitted from the east or west quarter are considered by themselves. The red, blue, and green arrows indicate additional baselines for MIMO data collected when pulses transmitted on two different antennas are considered together (see below).

(single input, multi output) mode when transmission is performed with either the east or west quarter alone. The red, blue, and green arrows, meanwhile, represent MIMO baselines when signals originating from different transmitting antennas are correlated. Note how additional baselines become available, some with redundancies. The red and blue lines correspond to two distinct spatial baselines measured in MIMO mode. The green lines are redundant, repeated-index baselines, V_{xy}^{ii}, with lengths equal to the displacement between the transmitting antennas. These are analagous to zero-baseline measurements in SIMO mode (not shown). Note that for every V_{xy}^{ij}, there is a V_{yx}^{ji} which will be redundant with one of the baselines already shown but which could be statistically independent when estimated, depending on how the experiment is performed.

Given N receiving antennas and M transmitting antennas, the total number of visibility measurements will be $MN(MN-1)/2$. Of these, $MN(N-1)/2$ are SIMO measurements (with repeated transmit antenna indices) representing up to just $N(N-1)/2$ independent baselines. That leaves $MN(M-1)N/2$ MIMO baselines. Of these, $NM(M-1)/2$ will have repeated receive antenna indices and represent up to just $M(M-1)/2$ distinct baselines. That leaves $MN(M-1)(N-1)/2$ additional MIMO baselines with distinct transmit and receive antenna indices plus the zero baseline. In the present implementation, there are 28 distinct SIMO baselines and 57 distinct MIMO baselines for a total, including the zero baseline, of 86.

The benefit of MIMO as implemented here is therefore a multiplicative increase in the number of interferometry baselines available (by a factor of essentially 3 in the case of two transmitting antennas). (As the imaging problem is an underdetermined one in most practical applications, more baselines is better.) This comes without the expense of adding receivers, receive antennas, and other associated hardware. Moreover, some of the new MIMO baselines will be longer than the longest SIMO baseline. **This is because the overall MIMO baseline lengths combine the receiving antenna displacements and the transmitting antenna displacements.**

The problem then becomes distinguishing signals which originated from different transmitting antennas. (Distinguishing signals from different receive antennas is no problem since each receive antenna has its own receiver and data stream.) As mentioned ear-

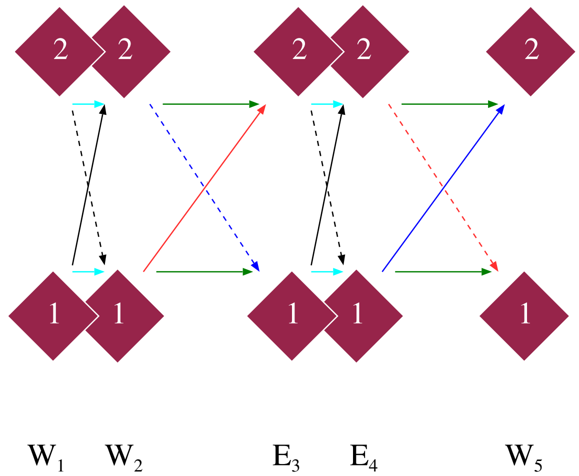

Figure 2. Diagram illustrating the sampling and formation of visibility estimates for the hypothetical two-antenna imaging case **employing time-division multiplexing**. The space depicted here is that of an abstract network, with the diamonds representing data streams acquired from the given antenna following pulse transmission from the given quarter. Here, baselines that share a color also share a spatial geometry. Dashes indicate V^{ij} with $i > j$ while green and cyan lines indicate $i = j$. Note that colors have different meanings in Figs. 1 and 2.

lier, this can be done in principle using polarization diversity or code diversity (see e.g., Urco et al., 2018). In the present case, the experiments were conducted using time diversity (or time division multiplexing), i.e., different antenna quarters were used for pulse transmission at different times. Specifically, we alternated transmitting antenna arrays from one pulse to the next following the sequence WWEEWWEE... Later we discuss the advantages and disadvantages of our implementation, but for now, given the relative large dynamic range as well as wide spectral characteristics of equatorial ionospheric irregularities, time diversity can be an expedient implementation.

Let us attach ordinal numbers to the pulses and write the sequence as $W_1W_2E_3E_4W_5$... for the sake of clarity. To process the data, we sort them into five streams, each containing every fourth sample in time beginning with W_1, W_2, E_3, E_4, and W_5, respectively. (Stream W_5 is identical to stream W_1 except delayed four samples in time.) Each of the streams is henceforth named according to its first sample. Each stream has an effective IPP four times the overall IPP or 4 ms in the present case. Each of the streams is then transformed from the time to the frequency domain by discrete Fourier transform.

The processing is illustrated in the diagram in Fig. 2 considering, again, the hypothetical two-antenna interferometer case for simplicity. MIMO measurements derive from correlating the W_2 and E_3 streams and the E_4 and W_5 streams. Note that a temporal lag as well as a spatial displacement is unavoidably inherent in these comparisons. For purposes of symmetry, the SIMO measurements will also incorporate temporal lags, i.e. they will derive from comparisons between the W_1 and W_2 streams and the E_3 and E_4 streams.

The normalized cross-spectra or visibilities V^{ij} for the SIMO measurements for receivers i and $j > i$ will consequently be:

$$
\begin{aligned}
2V^{ij}_{W_1W_2}(\omega) &= \frac{\langle v^i_{W_1}(\omega)v^{j*}_{W_2}(\omega)\rangle}{\sqrt{\langle v^i_{W_1}(\omega)v^{i*}_{W_2}(\omega)\rangle}\sqrt{\langle v^j_{W_1}(\omega)v^{j*}_{W_2}(\omega)\rangle}} &(1)\\
&+ \left(\frac{\langle v^j_{W_1}(\omega)v^{i*}_{W_2}(\omega)\rangle}{\sqrt{\langle v^j_{W_1}(\omega)v^{j*}_{W_2}(\omega)\rangle}\sqrt{\langle v^i_{W_1}(\omega)v^{i*}_{W_2}(\omega)\rangle}}\right)^* &(2)\\
2V^{ij}_{E_3E_4}(\omega) &= \frac{\langle v^i_{E_3}(\omega)v^{j*}_{E_4}(\omega)\rangle}{\sqrt{\langle v^i_{E_3}(\omega)v^{i*}_{E_4}(\omega)\rangle}\sqrt{\langle v^j_{E_3}(\omega)v^{j*}_{E_4}(\omega)\rangle}} &(3)\\
&+ \left(\frac{\langle v^j_{E_3}(\omega)v^{i*}_{E_4}(\omega)\rangle}{\sqrt{\langle v^j_{E_3}(\omega)v^{j*}_{E_4}(\omega)\rangle}\sqrt{\langle v^i_{E_3}(\omega)v^{i*}_{E_4}(\omega)\rangle}}\right)^* &(4)
\end{aligned}
$$

where the expectations are estimated by post-detection averaging (incoherent integration). One purpose of the normalization is to remove phase changes associated with temporal displacements, retaining only decorrelation and phase changes associated with spatial displacements.

Time series offset by time τ in the time domain will differ by a phase factor $\exp(i\omega\tau)$ in the Frequency domain. That factor could be removed from the visibility estimates as was done by Urco et al. (2019). However, if the signals are frequency aliased, which could be the case for the EEJ, ω here will be influenced by the aliased component of the power in the given frequency bin (Sahr et al., 1989). Our normalization scheme shown above accounts for any frequency aliasing that might be present in the decimated data.

Note that the four expressions on the right sides of Eq. 1 – 4 are four equivalent but independent estimators of the visibility for the interferometry baseline formed by receivers i and $j \geq i$. These are represented by the black arrows in Fig. 2. They must all be evaluated separately. Note that we do not actually estimate the value of the visibility for the zero baselines (with like i and j indices) as this is unity by definition. **(In our notation, the $j \leq i$ terms just repeat the terms already written.)**

Note also that noise estimation and removal is not part of these calculations. We assume the noise is uncorrelated in all the products in the equations above. This differs from conventional interferometry experiments where temporal displacements are not incorporated.

The new interferometry information afforded by MIMO concerning receivers i and $j \geq i$ comes from the following four additional estimators:

$$V^{ij}_{W_2E_3}(\omega) = \frac{\langle v^i_{W_2}(\omega) v^{j*}_{E_3}(\omega)\rangle}{\sqrt{\langle v^i_{W_1}(\omega) v^{i*}_{W_2}(\omega)\rangle}\sqrt{\langle v^j_{E_3}(\omega) v^{j*}_{E_4}(\omega)\rangle}} \quad (5)$$

$$V^{ji}_{W_2E_3}(\omega) = \frac{\langle v^j_{W_2}(\omega) v^{i*}_{E_3}(\omega)\rangle}{\sqrt{\langle v^j_{W_1}(\omega) v^{j*}_{W_2}(\omega)\rangle}\sqrt{\langle v^i_{E_3}(\omega) v^{i*}_{E_4}(\omega)\rangle}} \quad (6)$$

$$V^{ij}_{E_4W_5}(\omega) = \frac{\langle v^i_{E_4}(\omega) v^{j*}_{W_5}(\omega)\rangle}{\sqrt{\langle v^i_{E_3}(\omega) v^{i*}_{E_4}(\omega)\rangle}\sqrt{\langle v^j_{W_1}(\omega) v^{j*}_{W_2}(\omega)\rangle}} \quad (7)$$

$$V^{ji}_{E_4W_5}(\omega) = \frac{\langle v^j_{E_4}(\omega) v^{i*}_{W_5}(\omega)\rangle}{\sqrt{\langle v^j_{E_3}(\omega) v^{j*}_{E_4}(\omega)\rangle}\sqrt{\langle v^i_{W_1}(\omega) v^{i*}_{W_2}(\omega)\rangle}} \quad (8)$$

Here, the estimator in Eq. 5 corresponds to the solid red arrow in Fig. 2, Eq. 6 to the dashed blue arrow, Eq. 7 to the solid blue arrow, and Eq. 8 to the dashed red arrow. Note again that the estimators in Eq. 6 and Eq. 7 are redundant but statistically independent. The same is true for Eq. 5 and Eq. 8. So, there are twice as many MIMO baselines as SIMO baselines, but there are four independent estimators of each of the SIMO baselines compared with just two of each of the MIMO baselines.

Recall also that the visibilities in the MIMO analysis with common i and j indices represent finite interferometry baselines with the same spatial displacement as the transmitting antennas. This is depicted by the green horizontal arrows in Fig. 2. Measurements of MIMO visibilities with common indices are not only useful but are, in fact, crucial to the imaging method during calibration. We calibrate the phases of the receivers, which have random offsets associated with cabling differences, by identifying quasi point targets in the SIMO data and adjusting the individual receiver phase offsets for optimal focusing. The MIMO phases include an additional bias, however, associated with a potential phase difference between the two transmitting systems. (This difference is nulled manually in the field during experimental setup but cannot be removed completely.) Once the receiver phases have been calibrated, the transmit phase difference appears in the MIMO zero baseline measurements. From these, the bias can be estimated and negated.

Some peculiar attributes of the visibility measurements in our time diversity MIMO implementation warrant repetition. Visibility measurements with exchanged indices $i \Leftrightarrow j$ are not complex conjugate pairs as they are in conventional SIMO experiments. However, visibility measurements with exchanged indices and exchanged sequencing WE $\Leftrightarrow$ EW describe common spatial interferometry baselines and have expectations which are complex-conjugate pairs. Furthermore, the samples used for the WE measurements are distinct from those used for EW measurements, as illustrated in Fig. 2.

3 Imaging method with uncertainty analysis

The fundamental principles behind aperture synthesis imaging are well known and widely applied across astronomy and space physics. For a review, consult Thompson et al. (2017). In radar applications, images are constructed in every radar range and Doppler frequency bin. In each range bin, we take the scattered signal measured by an antenna at the spatial location $\mathbf{x}$ with Doppler frequency ω to be

$$v(\mathbf{x},\omega) = \int d\Omega\, E(\mathbf{k},\omega) e^{i\mathbf{k}\cdot\mathbf{x}} \tag{9}$$

where $\mathbf{E}$ is the amplitude of the far-zone electric field, $\mathbf{k}$ is the scattered wavevector, and $d\Omega$ is a differential solid angle interval. Correlating signals received at two separate locations then yields

$$\begin{aligned}\langle v(\mathbf{x}_1,\omega) v^*(\mathbf{x}_2,\omega)\rangle &= \left\langle \int d\Omega\, E(\mathbf{k},\omega) e^{i\mathbf{k}\cdot\mathbf{x}_1} \int d\Omega'\, E^*(\mathbf{k}',\omega) e^{-i\mathbf{k}\cdot\mathbf{x}_2} \right\rangle &(10)\\ &= \int d\Omega\, \langle |E(\mathbf{k},\omega)|^2\rangle e^{i\mathbf{k}\cdot(\mathbf{x}_1-\mathbf{x}_2)} &(11)\end{aligned}$$

Next, we assume the amplitudes of signals scattered from different bearings to be uncorrelated. We further assume that the scattering is spatially homogeneous such that the correlation on the left only depends on the difference between $\mathbf{x}_1$ and $\mathbf{x}_2$. Normalizing both sides of the equation by $\langle |v(\mathbf{x},\omega)|^2\rangle = \int d\Omega\, \langle E(\mathbf{k},\omega)|^2\rangle$ then gives

$$\begin{aligned}V(\delta\mathbf{x};k,\omega) &= \int d\Omega\, B(\mathbf{k},\omega) e^{i\mathbf{k}\cdot\delta\mathbf{x}}\\ &= \int d\eta d\xi \frac{B(\eta,\xi,\omega)}{\sqrt{(1-\eta^2-\xi^2)}} \exp\left\{ ik\left(\eta\delta x + \xi\delta y + \sqrt{1-\eta^2-\xi^2}\delta z\right)\right\} \quad (12)\end{aligned}$$

where we have defined the visibility $V(\delta\mathbf{x};k,\omega)$ and the brightness distribution $B(\eta,\xi)$. The integral over solid angles has been rewritten in terms of direction cosines η and ξ.

From Eq. 12, it is clear that the transformation between the measured visibility distribution and the sought-after brightness distribution is nearly a Fourier transform. In the event that all the antennas lie in a plane so that δz vanishes and that the imaging field of view is small so that the radical in the denominator of Eq. 12 is always nearly uniform, the transformation is a Fourier transformation exactly. In any event, Eq. 12 is a linear transformation.

Inverting Eq. 12 generally requires recourse to a statistical inverse method given that the visibility distribution will be irregularly and incompletely sampled in practice. In practice, the problem will also be underdetermined. At Jicamarca, the most often applied inverse method is rooted in the principle of maximum entropy (Wernecke & D'Addario, 1977; Skilling & Bryan, 1984; Wilczek & Drapatz, 1985). This is a regularization method which maximizes the entropy of the brightness distribution while holding the chi-square discrepancy between the predicted and measured visibilities to its expected value. The maximum entropy (MaxEnt) method finds the brightness distribution that is consistent with the measurements while being minimally committal to features without support in the data. The solution is restricted to positive values for the brightness distribution everywhere. The method is a super-resolution method and exceeds the diffraction limit. By the measure of Shannon's channel capacity theorem, no alternative method has a superior resolution (Jaynes, 1982; Kosarev, 1990).

In the discrete language of linear algebra, MaxEnt determines the brightness distribution b, which can be a vector of any size, by minimizing the objective function:

$$b = \underset{b}{\text{argmin}} \quad s + \lambda^T(Ab + e - v) - \Lambda(e^T C_d^{-1} e - \Sigma) \tag{13}$$

where s is the negative of the entropy of the brightness distribution, A is the linear transformation specified by Eq 12, v is the visibility data, e is a column vector of experimental errors, C_d is the visibility error covariance matrix, λ is a column vector of Lagrange multipliers, Λ is an additional Lagrange multiplier, and Σ is the expected chi-square value which is normally set to the number of visibility data. The term B is the sum of all the elements of b which is unity by definition for this problem. The optimization problem is one of maximizing the entropy of the brightness while constraining the chi-square parameter to equal its expectation.

Using standard optimization techniques, the minimum of the objective function can be shown to correspond to a brightness distribution with the following form:

$$
\begin{aligned}
s &= \sum_j b_j \ln(b_j/B) && (14) \\
b_j &= B\frac{e^{-\lambda^T A^{[,j]}}}{Z} && (15) \\
Z &= \sum_j e^{-\lambda^T A^{[,j]}} && (16)
\end{aligned}
$$

where Z plays the role of a partition function. Substituting this form back into Eq. 13 and minimizing with respect to the free parameters produces a system of n coupled equations for n Lagrange multipliers in terms of n real-valued data. The equations can be solved using conventional nonlinear solvers based on Levenberg-Marquardt methods. For details, see Hysell and Chau (2006).

An important aspect of the data inversion involves the specification of the data error covariance matrix C_d. For SIMO experiments, all the terms in C_d can be estimated using standard statistical methods (see e.g., Farley, 1969). The recipe for populating C_d is given in the appendix of Hysell and Chau (2006). That recipe remains applicable to visibility acquired in MIMO mode.

The error covariance matrix entry for visibility estimates V^{ij} and V^{kl} depends on the number of statistically independent samples, the signal-to-noise (SNR) ratio, and the products of the visibilities V^{ik}, V^{jl}, V^{il}, and V^{jk} in quadratic, cubic, and quartic combinations. In SIMO mode, estimates of all the required visibility permutations are made in the course of data processing. The same is true in MIMO mode, except that we must now distinguish not just the receive antenna number but also whether illumination came from the east or west antenna. We must also bear in mind that there are two distinct ways to estimate each MIMO interferometry baseline.

Suppose we desire the covariance between $V_{ab}^{ij} = (1/2)(V_{ab}^{ij} + V_{ba}^{ji*})$ and $V_{cd}^{kl} = (1/2)(V_{cd}^{kl} + V_{dc}^{lk*})$ where i, j, k, l are antenna numbers with $j \geq i$ and $l \geq k$ and a, b, c, d are either E or W. There are four cross terms to consider, each predicted individually by the four permuted visibilities written in the previous paragraph. That means sixteen terms in all, but these are redundant, and the overall covariance can be specified entirely in terms of $V_{ac}^{ik}, V_{bd}^{jl}, V_{ad}^{il}, V_{bc}^{jk}, j \geq i, l \geq k$. This formalism covers and is essentially no different than the strictly SIMO case except for the increased multiplicity of permuta-

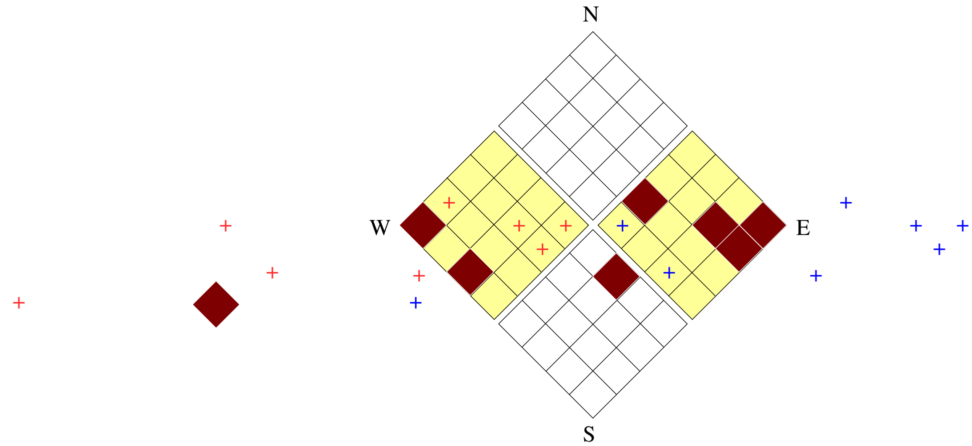

Figure 3. Plan view of the Jicamarca antenna array. Eight modules are used for reception (colored red) while two quarters are used for transmission (colored yellow). The reception modules were selected to provide a fairly uniform distribution of east-west interferometry baselines. Red and blue crosses indicate the positions of virtual antennas afforded by our time diversity MIMO mode.

tions. The only other consideration is that MIMO visibilities with repeated indices do not refer to the zero baseline as with SIMO.

4 Jicamarca example

A plan view of the Jicamarca antenna array is shown in Fig. 3. Eight independent modules are used for reception, and two quarters are used for transmission. The distance between the quarters is approximately 34 wavelengths. The longest baseline for SIMO (MIMO) processing is approximately 94 (128) wavelengths. The distribution of receiving antennas is elongated in the east-west direction deliberately. The magnetic field runs approximately north-south, and the Bragg scatter from field-aligned plasma density irregularities comes from the locus of perpendicularity which runs east-west in the figure. Images of the irregularities are very sharply concentrated in the plane perpendicular to the magnetic field, and baseline diversity in the east-west direction is consequently what is critical. Transmitting on the east and west quarters increases the longest east-west baseline and the diversity of east-west baselines on the whole. For SIMO (MIMO) processing, a total of 29 (86) interferometry baselines are available for imaging.

The point spread function (PSF) for the 29- and 86-baseline arrangements have been calculated in the high SNR limit assuming integration times consistent with the present

bin	29 baselines	86 baselines
-4	8.235e-07	
-3	8.258e-03	6.260e-04
-2	5.542e+00	1.537e+00
-1	2.543e+02	1.410e+02
0	2.476e+02	5.164e+02
1	2.476e+02	1.069e+02
2	1.275e+01	2.173e+00
3	1.241e-01	8.405e-03
4	4.365e-04	1.179e-05
5	8.235e-07	

Table 1. Point spread function for 29- and 86-baseline imaging configurations. The image space in this case spans 768 zenith angle bins, centered on bin 0, each 0.03° wide. All nonzero values within machine precision are shown.

experiments. To calculate the point spread fucntion, all visibilities were set to a value of unity, and their variances were taken to be uniform and independent. Images were computed on a 2D grid using 768 horizontal bins, and a cut was taken through the horizontal bisector. The results are shown in Table 1. **The profiles indicate how a point target would be resolved by the imaging algorithm given the number and lengths of baselines available in the two cases.** They indicate that the PSF is down by ∼15 dB in the ±2 bins for the SIMO configuration and about ∼25 dB in the MIMO configuration. Both configurations have PSF's that are confined essentially within ± 4 bins.

Coherent backscatter from plasma density irregularities in the equatorial electrojet are depicted in range-time-intensity format in Fig. 4. This is a conventional format for presenting comparable data, and the figure shown here is typical for observations obtained around twilight (Swartz & Farley, 1994; Farley et al., 1994). The figure is characterized by alternating, tilted bands of red- and blue-shifted echoes exhibiting a period of approximately 1 min. The bands are asymmetric, with the red-shifted bands being more prominent, intense, and faster than the blue-shifted bands. This behavior is typical for so-called "large scale waves" which are kilometer-scale waves created by gradi-

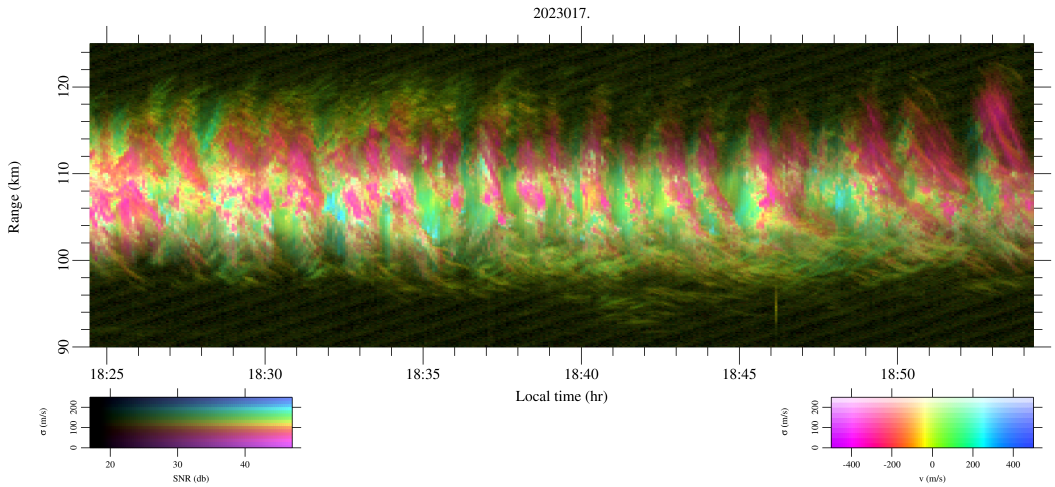

Figure 4. Range time intensity (RTI) representation of coherent scatter from plasma density irregularities in the equatorial electrojet. The brightness, hue, and saturation of the pixels indicate the SNR ratio, Doppler shift, and spectral width of the echoes, respectively, according to the legends shown. (Red/blue hues denote red/blue shifts, respectively.) The time resolution is 5 s, and the range resolution is 150 m. Local times are shown.

ent drift instability in the electrojet region. The waves increase in wavelength between daytime and nighttime and tend to aperiodic behavior around the postsunset reversal of the background zonal electric field. The theory of large-scale waves has been discussed at length by Kudeki et al. (1982); Pfaff et al. (1987); Ronchi et al. (1989, 1991); Hu and Bhattacharjee (1999); Hysell and Chau (2002). Large-scale wave are perhaps among the best understood phenomena in equatorial aeronomy as the congruity of observations, including those presented here, and numerical simulations is excellent. Questions remain nonetheless including the precise nature of the coupling between gradient drift and Farley Buneman waves, anomalous effects of gradient drift waves on transport, and the role of sporadic E layers in the electrojet (Ronchi, 1990). These questions prompt efforts to improve our experimental methods.

The plasma density irregularities under study here are strongly magnetic field aligned, and all of the backscatter comes from the plane in which the scattering wavevector is normal to the background magnetic field (Kudeki & Farley, 1989). Although our radar images are constructed in two dimensions, we consider 1D cuts through the locus of perpendicularity, stacking the results in range to produce 2D images. Each Doppler bin is processed separately, and the results are combined by plotting pixels with brightness,

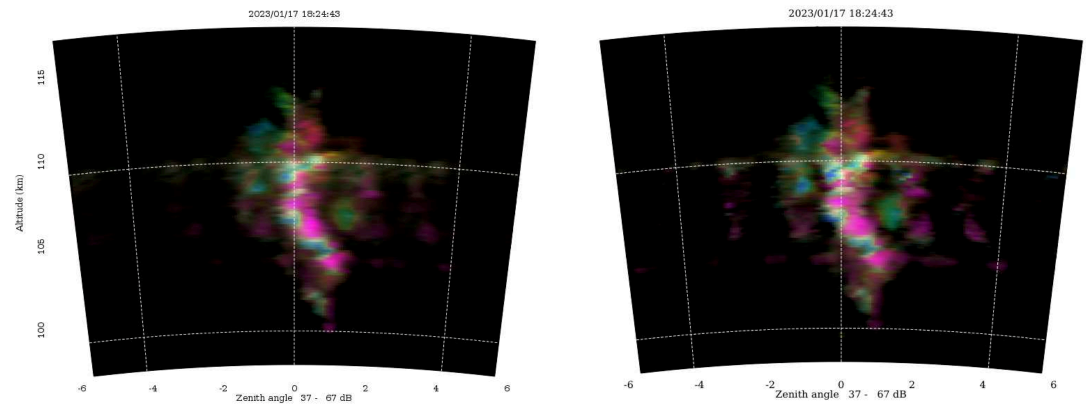

Figure 5. Comparison of representative images formed using 29 interferometry baselines in SIMO mode (left) and 86 baselines in MIMO mode (right).

hue, and saturation being indicative of the SNR, Doppler shift, and spectral width in the given range-azimuth angle cell.

Fig. 5 shows a comparison between images computed using 29 interferometry baselines in SIMO mode and 86 baselines in MIMO mode. The images represent five seconds of incoherent integration time. A Doppler spectrum has been computed behind each pixel, and the pixel brightness, hue and saturation are indicative of the SNR, Doppler shift, and spectral width, respectively. The span of within-the-pixel SNRs depicted is 37–67 dB. Doppler velocities span ± 375 m/s with blue (red) tones denoting blue (red) shifts. That the backscatter arrives mainly from the horizontal center of the images is a consequence of the beamwidth and radiation pattern of the transmitting antenna quarters.

Differences between the two panels in Fig. 5 are subtle in view of the broad span of SNRs depicted, but they are unmistakable. **The detail in the MIMO-mode panel is greater, and fine structure at the boundaries of color islands in particular is more clearly defined. The level of detail in the MIMO image is most obviously greater around 110 km range where structure at the individual pixel level becomes apparant.** The MIMO SNRs are slightly greater as the imaging algorithm is more able to concentrate power in occupied pixels and exclude it from unoccupied ones.

Fig. 6 shows sequences of contiguous images computed in SIMO (left) and MIMO (right) mode. The images continue to represent five-second incoherent integration times

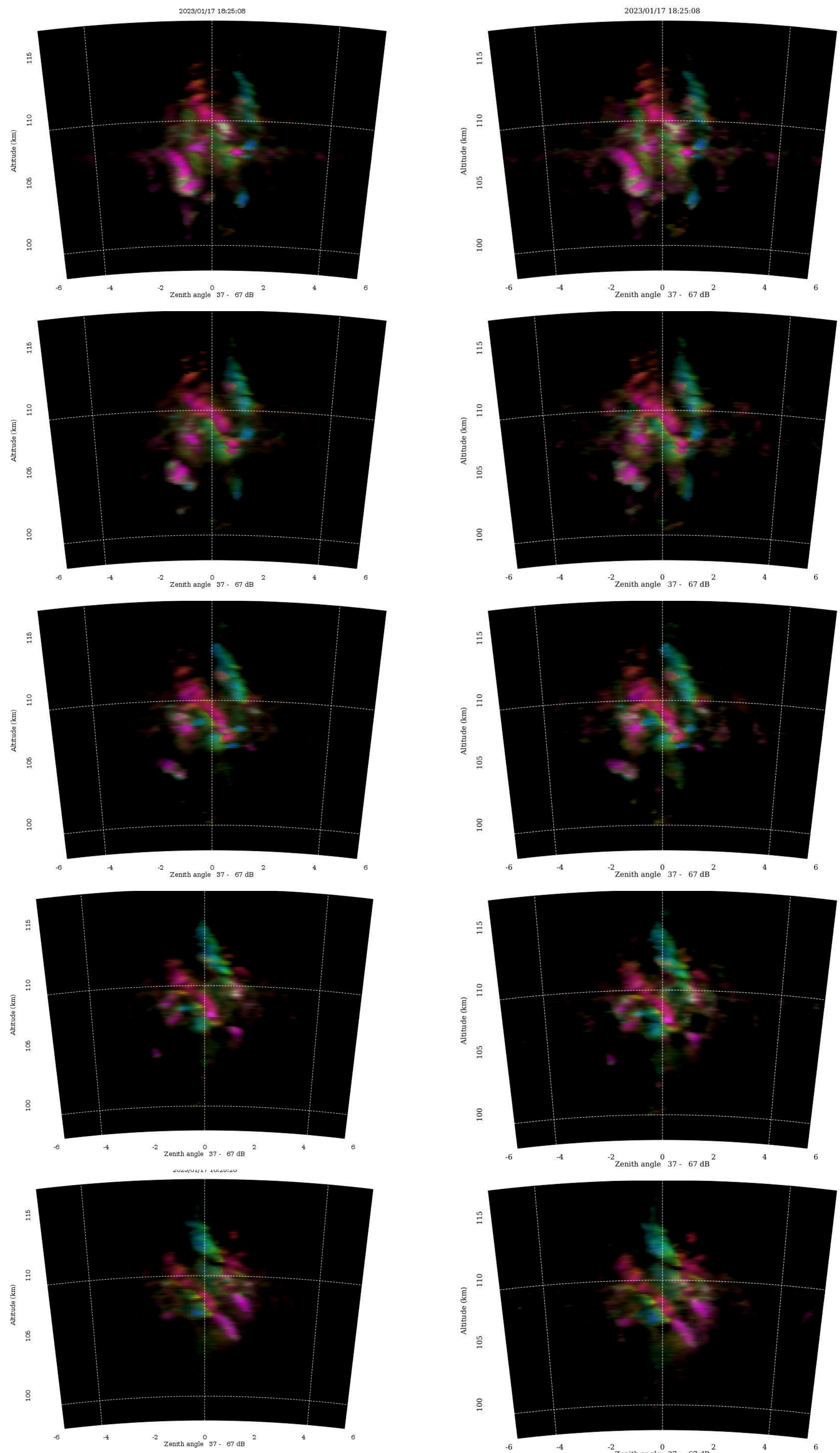

Figure 6. Similar to Fig. 5 but for a contiguous sequence of images from top to bottom.

and are spaced by five seconds. The images depict the propagation of large-scale gradient drift waves propagating from east to west and downward with time. The red-shifted phases of the waves are brighter and more distinct than the blue-shifted phases. Long, animated sequences of images show that the wave period is approximately one minute such that about half a period is depicted in Fig. 6. The figure also shows secondary wave features superimposed on the primary waves. There is considerable fine structure in the imagery which is more discernible in MIMO mode than in SIMO mode. The motion of the wavefronts is sufficiently rapid to introduce smearing in the images as well, however, and this most likely contributes as much distortion to the images as the finite aperture size in either SIMO or MIMO mode. Dynamic distortion like this could be reduced with the adoption of shorter incoherent integration times, but that would increase the variances of the visibility data and reduce the image sharpness accordingly. The images presented here represent an attempt to find an optimal balance.

5 Summary and Evaluation

This paper considered the theory and application of time diversity MIMO for aperture synthesis radar imaging. The specific application was to VHF coherent scatter from the EEJ, but the treatment has been sufficiently general to apply broadly to volume scatter. Incorporating MIMO into the imaging methodology allows all of the degrees of freedom available in radar experiments (i.e. range, time, Doppler frequency, receiver diversity, and transmitter diversity) to be exploited.

For the most part, incorporating MIMO methods in imaging represents an incremental change in the algorithm coding, although the bookkeeping is considerably more complicated, and the computational cost is considerably greater. The computational cost of the method described here, i.e., with MaxEnt, are essentially $\mathcal{O}(n^3)$ where n is the number of visibility measurements. Increasing the number of baselines therefore increases computation time considerably, although this can be mitigated in large part by parallelization. The algorithm scales efficiently in view of the fact that images for different range and Doppler bins can be formed using independent threads.

The adoption of MIMO methods in radar imaging is a question in a complicated trade space. **MIMO increases both the number and maximum length of interferometry baselines without the need for additional hardware or real estate.**

This can improve the fidelity and resolution of aperture synthesis imagery over SIMO methods. The improvement comes at the cost of additional coding complexity and computation time, as mentioned above.

Perhaps most importantly, the time diversity strategy employed for this work reduces the SNR by a factor of four in the present case. While the SNR (per range gate) for the EEJ echoes was very high, on the order of 50 dB at times and in places, the 6 dB reduction is not insignificant in imaging applications. (This can be contrasted with many other radar applications where increasing the signal-to-noise ratio (SNR) beyond about 10 dB often has little effect on downstream confidence intervals (Farley, 1969)). Kosarev (1990) showed that the resolution improvement of the aperture synthesis analysis described here is predicted by Shannon's channel capacity theorem, i.e.

$$R = \frac{1}{3}\log_2(1 + S/N) \tag{17}$$

where R is the multiplicative improvement in the imaging resolution compared to the diffraction limit which, in turn, is set by the longest interferometry baseline length. The latter increased by a factor of 1.36 with the introduction of MIMO methods in the Jicamarca experiment. This factor is completely offset by the decrease in S/N by 6 dB when the SNR falls below 22.7 dB. As all of the echoes shown in this paper were stronger than this, MIMO was always advantageous, although the reduction in SNR blunted the improvement even for the strongest echoes. Not only the maximum length but also the number of interferometry baselines contribute to overall image quality, however, and cost/benefit ratio of MIMO is more complicated than this and hard to quantify.

The MIMO implementation described in this paper is therefore only beneficial in the high signal-to-noise limit. If the signal strength is sufficient, it could be advantageous to adopt more than two transmitter locations. This strategy could be used to implement an enormous number of interferometry baselines which could be advantageous, for example in 2D imaging applications involving a large number of compact targets.

Using time diversity has a few advantages over code diversity along with a number of disadvantages. The former is comparatively easy to implement in experiments and is more resilient to clutter associated with range sidelobes. Note that the MaxEnt algorithm only fails to converge in practice when range clutter is substantial as can sometimes happen with targets with high dynamic range like the EEJ. The disadvantages of time diversity compared to code diversity are a reduced duty cycle, reduced effective IPP, reduced SNR, and increased analysis complexity. **These disadvantages could be highly detrimental in some applications, the study of overspread targets like plasma density irregularities associated with equatorial spread *F* (ESF) for example. For overspread targets, increasing the effective IPP may not be a practical option.** In most circumstances, where code diversity is possible, it will outperform time diversity.

Finally, there are a number of ways to improve the experiment described in this paper. For one, the PRF could be increased somewhat in view of the limited altitude range of the EEJ echoes. This would reduce or eliminate the possibility of frequency aliasing. For another, the width of the imaging region over Jicamarca could be increased by spoiling the transmit antenna beam to illuminate a broader sector in the EEJ. In similar experiments conducted in the past, this permitted the rendering of multiple wavelengths of the large-scale waves overhead (Hysell & Chau, 2002). Finally, we note that the EEJ images presented in this paper suffered non-negligible smearing due to the horizontal motion of the irregularities being illuminated. In view of the apparent horizontal speeds of the scatterers, the smearing was comparable to the effects of the finite aperture size. In the future, the effects of horizontal motion could be largely removed using one of a number of adaptive filtering methods (e.g., Du et al., 2015; Ma, 2020). The experimental and computational cost-to-benefit ratio would seem to be attractive compared to further refinements in the static imaging methodology.

Acknowledgments

The Jicamarca Radio Observatory is a facility of the Instituto Geofisíco del Perú operated with support from NSF award AGS-2213849 through Cornell. The help of the staff is much appreciated.

Open Research Data used for this publication are available through Hysell and Chau [2023].

References

Bahcivan, H., Hysell, D. L., Lummerzheim, D., Larsen, M. F., & Pfaff, R. F. (2006). Observations of collocated optical and radar auroras. *J. Geophys. Res.*, *111, A12308*, doi:10.1029/2006JA011923.

Bui, M. X., Hysell, D. L., & Larsen, M. F. (2023). Midlatitude sporadic E-layer horizontal structuring modulated by neutral instability and mixing in the lower thermosphere. *J. Geophys. Res.*, *128*(e2022JA030929), https://doi.org/10.1029/2022JA030929.

Chau, J. L., Urco, J. M., Avsarkisov, V., Vierinen, J. P., Latteck, R., Hall, C. M., & Tsutsumi, M. (2020). Four-dimensional quantification of Kelvin-Helmholtz instabilities in the polar summer mesosphere using volumetric radar imaging. *Geophys. Res. Lett.*, *47*, https://doi.org/10.1029/2019GL086081.

Chau, J. L., Urco, J. M., Pekka Vierinen, J., Andrew Volz, R., Clahsen, M., Pfeffer, N., & Trautner, J. (2019). Novel specular meteor radar systems using coherent MIMO techniques to study the mesosphere and lower thermosphere. *Atmospheric Measurement Techniques*, *12*(4), 2113–2127. doi: 10.5194/amt-12-2113-2019

Chau, J. L., Urco, J. M., Vierinen, J., Harding, B. J., Clahsen, M., Pfeffer, N., ... Erickson, P. J. (2021). Multistatic Specular Meteor Radar Network in Peru: System Description and Initial Results. *Earth and Space Science*, *8*(1), e01293. doi: 10.1029/2020EA001293

Du, H., Wang, W., & Bai, L. (2015). Observation noise modeling based particle filter: An efficient algorithm for target tracking in glint noise environment. *Neurocomputing*, *158*, 155-166. Retrieved from `https://www.sciencedirect.com/science/article/pii/S0925231215001046` doi: https://doi.org/10.1016/j.neucom.2015.01.057

Farley, D. T. (1969). Incoherent scatter correlation function measurements. *Radio Sci.*, *4*, 935-953.

Farley, D. T., Ierkic, H. M., & Fejer, B. G. (1981). Radar interferometry: A new technique for studying plasma turbulence in the ionosphere. *J. Geophys. Res.*, *86*, 1467–1472.

Farley, D. T., Swartz, W. E., Hysell, D. L., & Ronchi, C. (1994). High-resolution radar observations of daytime kilometer-scale wave structure in the equatorial electrojet. *J. Geophys. Res.*, *99*, 299.

Frazer, G. J., Abramovich, Y. I., & Johnson, B. A. (2007). Spatially waveform diverse radar: Perspectives for high frequency othr. In *2007 ieee radar conference* (p. 385-390). doi: 10.1109/RADAR.2007.374247

Harding, B. J., & Milla, M. A. (2013, October). Radar imaging with compressed sensing. *Radio Sci.*, 582–588, DOI: 10.1002/rds.20063.

He, Z., Chen, G., Yan, C., Zhang, S., Yang, G., & Li, Y. (2023). Imaging radar observations of the daytime F-region irregularities in low-latitudes of China. *J. Geophys. Res.*, *128*(e2022JA030878), https://doi.org/10.1029/2022JA030878.

Hu, S., & Bhattacharjee, A. (1999). Gradient drift instabilities and turbulence in the nighttime equatorial electrojet. *J. Geophys. Res.*, *104*(A12), 28,123–18,132.

Huang, Y., Brennan, P. V., Patrick, D. E., Weller, I., Roberts, P., & Hughes, K. (2011). Fmcw based mimo imaging radar for maritime navigation. *Progress in Electromagnetics Research-pier*, *115*, 327-342.

Huyghebaert, D., Clahsen, M., Chau, J. L., Renkwitz, T., Latteck, R., Johnsen, M. G., & Vierinen, J. (2022). Multiple E-Region Radar Propagation Modes Measured by the VHF SIMONe Norway System During Active Ionospheric Conditions. *Frontiers in Astronomy and Space Sciences*, *9*(May), 1–16. doi: 10.3389/fspas.2022.886037

Hysell, D. L. (1996). Radar imaging of equatorial *F* region irregularities with maximum entropy interferometry. *Radio Sci.*, *31*, 1567.

Hysell, D. L., & Chau, J. L. (2002). Imaging radar observations and nonlocal theory of large-scale waves in the equatorial electrojet. *Ann. Geophys.*, *20*, 1167.

Hysell, D. L., & Chau, J. L. (2006). Optimal aperture synthesis radar imaging. *Radio Sci.*, *41*, 10.1029/2005RS003383, RS2003.

Hysell, D. L., & Chau, J. L. (2012). Aperture synthesis imaging for upper atmospheric research. In J. Bech & J. L. Chau (Eds.), *Doppler radar observations - weather radar, wind profiler, ionospheric radar, and other advanced applications* (p. DOI: 10.5772/39024). InTech.

Hysell, D. L., & Chau, J. L. (2023). Jan. 2023 EEJ dataset. [Dataset], JRO Database, https://www.igp.gob.pe/observatorios/radio-observatorio-jicamarca/database/dataset/2023-january-16-18-imaging-intermediate-data

Hysell, D. L., Yamamoto, M., & Fukao, S. (2002). Imaging radar observations and theory of type I and type II quasi-periodic echoes. *J. Geophys. Res.*, *107 (A11)*, 1360.

Jaynes, E. T. (1982). On the rationale of maximum-entropy methods. *Proc. IEEE*, *70*, 939.

Kosarev, E. L. (1990). Shannon's superresolution limit for signal recovery. *Inverse Problems*, *6*, 55–76.

Kudeki, E., & Farley, D. T. (1989). Aspect sensitivity of equatorial electrojet irregularities and theoretical implications. *J. Geophys. Res.*, *94*, 426.

Kudeki, E., Farley, D. T., & Fejer, B. G. (1982). Long wavelength irregularities in the equatorial electrojet. *Geophys. Res. Lett.*, *9*, 684.

Kudeki, E., & Sürücü, F. (1991). Radar interferometric imaging of field-aligned plasma irregularities in the equatorial electrojet. *Geophys. Res. Lett.*, *18*, 41.

Larsen, M. F., Hysell, D. L., Zhou, Q. H., Smith, S. M., Friedman, J., & Bishop, R. L. (2007). Imaging coherent scatter radar, incoherent scatter radar, and optical observations of quasiperiodic structures associated with sporadic *E* layers. *J. Geophys. Res.*, *112, A06321*, doi:10.1029/2006JA012051.

Ma, Y. (2020, jan). A research on dynamic target tracking with camera based on kalman filter. *Journal of Physics: Conference Series*, *1453*(1), 012106. Retrieved from `https://dx.doi.org/10.1088/1742-6596/1453/1/012106` doi: 10.1088/1742-6596/1453/1/012106

Matsuda, T., & Hashiguchi, H. (2023). Ddma-mimo observations with the mu radar: Validation by measuring a beam broadening effect. *IEEE Journal of Selected Topics in Applied Earth Observations and Remote Sensing*, *16*, 3083-3091. doi: 10.1109/JSTARS.2023.3258139

Pfaff, R. F., Kelley, M. C., Kudeki, E., Fejer, B. G., & Baker, K. D. (1987). Electric field and plasma density measurements in the strongly driven daytime equatorial electrojet, 1, The unstable layer and gradient drift waves. *J. Geophys. Res.*, *92*, 13,578.

Ronchi, C. (1990). *Large scale turbulence in the equatorial electrojet* (Unpublished doctoral dissertation). Cornell Univ., Ithaca, N. Y.

Ronchi, C., Similon, P. L., & Sudan, R. N. (1989). A nonlocal linear theory of the gradient drift instability in the equatorial electrojet. *J. Geophys. Res.*, *94*, 1317.

Ronchi, C., Sudan, R. N., & Farley, D. T. (1991). Numerical simulations of large-scale plasma turbulence in the daytime equatorial electrojet. *J. Geophys. Res.*, *96*, 21,263.

Sahr, J. D., Farley, D. T., & Swartz, W. E. (1989). Removal of aliasing in pulse-to-pulse Doppler radar measurements. *Radio Sci.*, *24*, 697.

Saito, S., Yamamoto, M., & Hashiguchi, H. (2008). Imaging observations of nighttime mid-latitude F-region field-aligned irregularities by an MU radar ultra-multi-channel system. *Ann. Geophys.*, *26*, 2345–2352.

Skilling, J., & Bryan, R. K. (1984). Maximum entropy image reconstruction: General algorithm. *Mon. Not. R. Astron. Soc.*, *211*, 111.

Sommer, S., & Chau, J. L. (2016). Patches of polar mesospheric summer echoes characterized from radar imaging observations with MAARSY. *Ann. Geophys.*, *34*(12), 1231–1241.

Swartz, W. E., & Farley, D. T. (1994). High-resolution radar measurements of turbulent structure in the equatorial electrojet. *J. Geophys. Res.*, *99*, 309.

Thompson, A. R., Moran, J. M., & Jr., G. W. S. (2017). *Interferometry and synthesis in radio astronomy, 3rd ed.* New York: John Wiley.

Urco, J. M., Chau, J. L., Milla, M. A., Vierinen, J. P., & Weber, T. (2018). Coherent MIMO to improve aperture synthesis radar imaging of field-aligned irregularities: First results at Jicamarca. *IEEE Trans. Geosci. and Remote Sens.*, *56*(5), 2980–2990, doi:10.1109/TGRS.2017.2788425.

Urco, J. M., Chau, J. L., Weber, T., & Latteck, R. (2019). Enhancing the spatiotemporal features of polar mesosphere summer echoes using coherent mimo and radar imaging at maarsy. *Atmospheric Measurement Techniques*, *12*(2), 955–969. Retrieved from `https://www.atmos-meas-tech.net/12/955/2019/` doi: 10.5194/amt-12-955-2019

Wernecke, S. J., & D'Addario, L. R. (1977). Maximum entropy image reconstruction. *IEEE Trans. Computers*, *c-26*, 351.

Wilczek, R., & Drapatz, S. (1985). A high accuracy algorithm for maximum entropy image restoration in the case of small data sets. *Astron. Astrophys.*, *142*, 9.

Zheng, L., & Tse, D. (2003). Diversity and multiplexing: a fundamental tradeoff in multiple-antenna channels. *IEEE Transactions on Information Theory*, *49*(5), 1073-1096. doi: 10.1109/TIT.2003.810646